

Takahiro Nagata

National Institute for Materials Science, Tsukuba, Japan

15.1 Introduction

The transparent semiconducting oxide (TSO) indium oxide (In_2O_3) is a wide-bandgap semiconducting material with a direct bandgap around 2.8–2.9 eV [1,2], although a recent study suggests a slightly indirect bandgap [3]. In_2O_3 -based oxides are already used as transparent conducting oxides (TCOs). High tin (Sn)-doped In_2O_3 (ITO) shows a high electrical conductivity with transparency in the visible range. ITO films on glass can be easily fabricated at relatively low temperatures compared to other oxides such as SnO_2 or ZnO . ITO is drawing attention and has been widely used as transparent electrodes for flat-panel displays and solar cells. The current research in TCOs seeks superior properties of low resistivity and high mobility [4–7]. Consumer demand for enlarged display size and/or tandem-structure photovoltaics with sensitivity in a wide range of spectral regions of the sun is strongly accelerating this search.

In contrast to TCOs, unintentionally doped In_2O_3 has a gas-sensing ability due to a surface electron accumulation layer (SEAL) [8], but for applications such as Schottky diodes and field-effect transistors (FETs) the SEAL should be controlled. Some groups report the removal of the SEAL by an O-plasma or O-rich sputtering atmosphere [9–11]. The SEAL is observed not only in In_2O_3 but also in other wide-bandgap semiconducting oxides such as SnO_2 [12] and ZnO [13]. Many efforts have been undertaken to remove the SEAL from binary semiconductors such as ZnO , InN , and InAs by chemical and/or physical surface treatments [14,15], and the origins of the SEAL have been proposed to be metal adatoms, surface oxygen vacancies, and adsorbates [16,17].

Relating to the control of vacancies, electrical properties including the polarity of n-type or p-type conductivity and carrier density are investigated for various applications such as transparent transistors [18,19], optoelectronic devices [20,21], and spin-electronic devices [22]. For example, the FET requires a channel with high mobility and moderate carrier concentration, a Schottky contact or gate insulator as control gate, and low resistance source and drain regions.

For electronic device applications, most In_2O_3 films were grown on glass at low temperature with a polycrystalline and/or amorphous crystalline structure. However, to understand the potential and functions of the material, single crystals or epilayers are the model systems. This chapter focuses on In_2O_3 single crystalline, high-quality, thin film material only.

15.2 Crystal growth

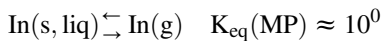
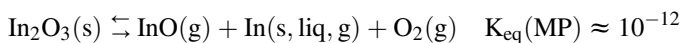
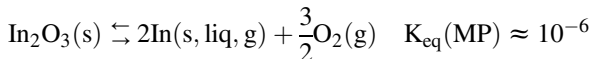
15.2.1 Thermodynamic properties and definition of usable growth methods

In_2O_3 is less stable than other wide bandgap oxides, such as ZnO and Ga_2O_3 . Indium has long been known to form two oxides, In_2O_3 and In_2O [23]; In_2O is a gaseous oxide. Burns et al. investigated the vaporization of In_2O_3 by mass spectrometric study [24], suggesting that $\text{In}_2\text{O} \rightarrow \text{In}^+ + \text{InO} + e$ is energetically more favorable. In contrast, In_2O_3 (solid) $\rightarrow \text{In}_2\text{O}_3$ (gas) would be independent of the partial oxygen pressure in the carrier gas, with the pressure measured by the transport method. Valderrama reported that In and In_2O are the important species in the vapor phase, rather than the $\text{In} + \text{In}_2\text{O}_3$ mixture. The vapor pressure of In_2O corresponds to the reaction $4\text{In} + \text{In}_2\text{O}_3 \rightarrow 3\text{In}_2\text{O}$ in the temperature range of 600–950°C [25]. This was confirmed by Nicholas, suggesting that no identification of the solid In_2O and In -rich condition is easily from the oxygen vacancies in In_2O_3 [26].

In contrast, In_2O_3 has polymorph phases, a bixbyite-type structure, body-centered cubic (bcc-, space group $\text{Ia}\bar{3}$) shape with lattice parameter of $a = 10.117 \text{ \AA}$, and a corundum-type, rhombohedral (rh-, space group $\text{R}\bar{3}\text{c}$) polymorph with lattice parameters $a = 5.487 \text{ \AA}$, $c = 14.510 \text{ \AA}$ structure [27–29], as shown in Fig. 15.1. The trivalent rare-earth sesquioxides tend to crystallize in the bcc-structure, and the transition metal sesquioxides assume the rh-structure. For In_2O_3 , the structural relations between bixbyite and corundum have attracted significant attention. The high-pressure, high-temperature synthesis of corundum-type In_2O_3 was reported in the 1960s [30–32], meaning that corundum-type In_2O_3 is a metastable phase. Under normal conditions In_2O_3 crystallizes in a bixbyite-type structure.

In even the most stable bixbyite-type structure, In_2O_3 is less stable than other wide-bandgap oxides for single crystal growth. When dealing with the single crystal growth of metal oxides, the decomposition of both the melt and the crystalline phase should be suppressed at temperatures close to the melting point. However, the chemical instability of In_2O_3 causes decomposition and massive evaporation at elevated temperatures much below melting point. To understand these evaporation conditions, Galazka et al. reported thermodynamic calculations using Fact Sage software [33], as shown in Fig. 15.2 [34].

The reactions are set as follows:



where (s) stands for solid, (liq) for liquid, (g) for gas, K_{eq} for equilibrium constant, and MP for melting point. The results indicate that the decomposition of In_2O_3 will occur upon heating up, and the most volatile species will be In and O_2 . To reduce In_2O_3

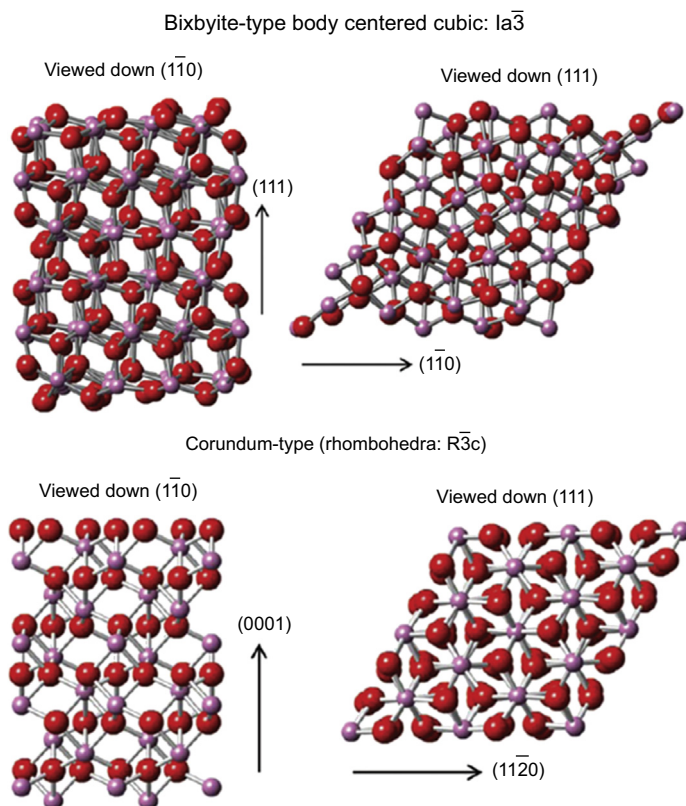


Figure 15.1 Ball-and-stick representations of crystal structures of $\text{bcc-In}_2\text{O}_3$ (upper panels) and $\text{rh-In}_2\text{O}_3$ (lower panels). In atoms are pink and O atoms are dark red. The viewing directions and the in-plane orientation are indicated in the figure.

Reprinted with permission from K.H.L. Zhang, V.K. Lazarov, P.L. Galindo, F.E. Oropenza, D.J. Payne, H.H.-C. Lai, R.G. Egdell, Domain matching epitaxial growth of In_2O_3 thin films on $\alpha\text{-Al}_2\text{O}_3(0001)$, *Cryst. Growth Des.* 12 (2012) 1000–1007. Copyright (2012) by the American Chemical Society.

decomposition, high oxygen partial pressure is effective; this is achieved by changing the oxygen partial pressures provided by two different oxygen sources, ($\text{O}_2 + \text{Ar}$) and CO_2 . CO_2 dynamically releases oxygen with increasing temperature, so oxygen partial pressure can be achieved by employing CO_2 at pressures above 100 bars. Nevertheless, even such high oxygen partial pressure is not sufficient to minimize In_2O_3 decomposition to the level needed for carrying out the typical Czochralski method and perhaps all other standard melt growth techniques.

15.2.2 Bulk single crystal growth

The thermodynamic calculations revealed that with conventional standard melt growth it is hard to obtain bulk single crystal In_2O_3 . In contrast, for $\beta\text{-Ga}_2\text{O}_3$ three different

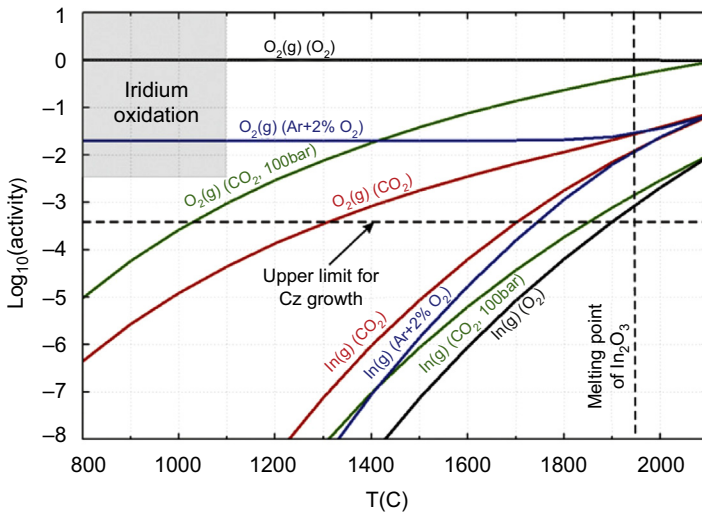
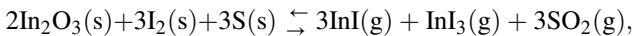


Figure 15.2 Partial pressure of the most volatile component (In) during In_2O_3 decomposition versus oxygen partial pressure provided by two different oxygen sources, (Ar + O_2) and CO_2 . Reprinted with permission from Z. Galazka, R. Uecker, K. Irmischer, D. Schulz, D. Klimm, M. Albrecht, M. Pietsch, S. Ganschow, A. Kwasniewski, R. Fornari, Melt growth, characterization and properties of bulk In_2O_3 single crystals, *J. Cryst. Growth* 362 (2013) 349–352. Copyright (2011) by Elsevier.

melt growth techniques can be used: Verneuil [35–37], optical floating zone [38–40], and the Czochralski method [41,42]. Instead of a melt growth technique, in early years the chemical vapor transport (CVT) method ([43,44]) was used for In_2O_3 bulk single crystals [45,46]. The advantage of CVT is the low growth temperature, below the melting temperature. Instead of vaporizing a solid directly at high temperatures, highly volatile chemicals are vaporized at much lower temperatures and react back the resulting gas mixture at a different temperature using the temperature dependence of the chamber. The reactions are easy to calculate by thermodynamic considerations. Scherer used pure powder of In_2O_3 and iodine and sulfur as the transport agents [47]. The chemical reaction is as follows:



where (s) and (g) denote solid and gaseous, respectively. The forward reaction describes the formation of the constituents to the transport medium, and the backward reaction describes its decomposition into In_2O_3 single crystals and transport gases. By this technique, growth of In_2O_3 crystals with a typical size of $3 \times 3 \times 1 \text{ mm}^3$ has been demonstrated, as shown in Fig. 15.3(a) [48].

To obtain larger In_2O_3 crystals than those grown by CVT, Galazka et al. applied a new melt growth technique, levitation-assisted self-seeding crystal growth method (LASSCGM), to In_2O_3 [49]. LASSCGM involves electromagnetic levitation, which uses a radiofrequency coil surrounding a metal crucible. There are an oxide melt

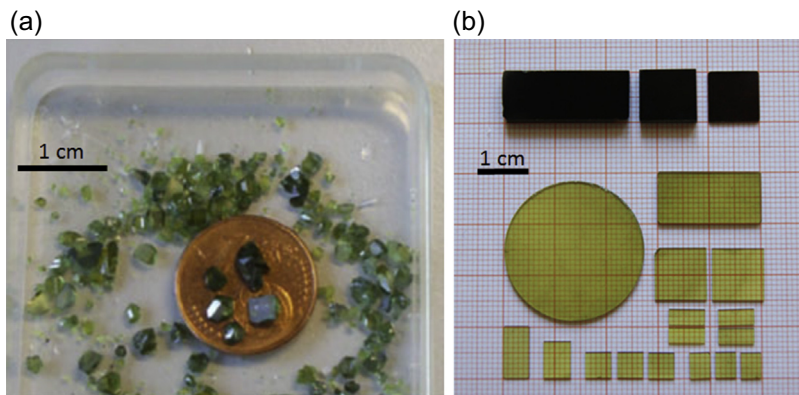


Figure 15.3 Photograph of In_2O_3 bulk single crystal grown from (a) CVT and (b) melt (upper: as grown; bottom: annealed).

(a) Reprinted from D. Braun, V. Scherer, C. Janowitz, Z. Galazka, R. Fornari, R. Manzke, In-gap states of In_2O_3 single crystals investigated by scanning tunneling spectroscopy, *Phys. Status Solidi A* (2013) 1–7, copyright (2013), with permission from WILEY-VCH. (b) Reprinted from Z. Galazka, R. Uecker, K. Irmischer, D. Schulz, D. Klimm, M. Albrecht, M. Pietsch, S. Ganschow, A. Kwasniewski, R. Fornari, Melt growth, characterization and properties of bulk In_2O_3 single crystals, *J. Cryst. Growth* 362 (2013) 349–352, copyright (2011), with permission from Elsevier.

and a self-created seed inside the crucible. The levitation has two functions: it drags the melt away from the hottest region, where there is the highest probability of eutectic formation with the metal crucible, and it forms the thin seed necessary to obtain a single crystal. To function, the metal excess must be sufficient to turn the insulating charge into a conductive charge and speed up the melting via direct coupling of the charge material with the electromagnetic field generated by the radio frequency coil. When approaching the melting point, which is about 1950°C , the decomposition rate of In_2O_3 increases, inducing the In-rich conditions which enhance conduction. To keep these conditions, oxygen concentration is limited. Based on the thermodynamic calculation, CO_2 was used as an oxygen source to grow In_2O_3 , and oxygen concentration was controlled at the level of several percentage points, typically 2%–6%. Growth of larger In_2O_3 crystals has been achieved, as shown in Fig. 15.3(b) [34]. The full width at half maximum value of the X-ray diffraction rocking curve of 222 peak on the (111) face of the In_2O_3 crystal was measured to be as low as 28 arcsec. As-grown crystals showed dark coloration with typical free electron concentrations of $1.8\text{--}3.1 \times 10^{18} \text{ cm}^{-3}$, and free electron mobility ranging from 135 to $170 \text{ cm}^2/\text{Vs}$. After annealing in a nonreducing atmosphere (neutral and oxidizing) for 5–120 h at temperatures between 700 and 1400°C , the electron concentrations were decreased by one order of magnitude. Typical free electron concentrations and free electron mobility were of $1.3\text{--}3.6 \times 10^{17} \text{ cm}^{-3}$ and $130\text{--}180 \text{ cm}^2/\text{Vs}$, respectively. The transmission electron microscope (TEM) observation on the (111) melt-grown In_2O_3 crystal revealed a defect-free and high-perfection crystal structure, as shown in Fig. 15.4(a). On this (111) melt-grown In_2O_3 crystal, Sadofev demonstrated the epitaxial growth of

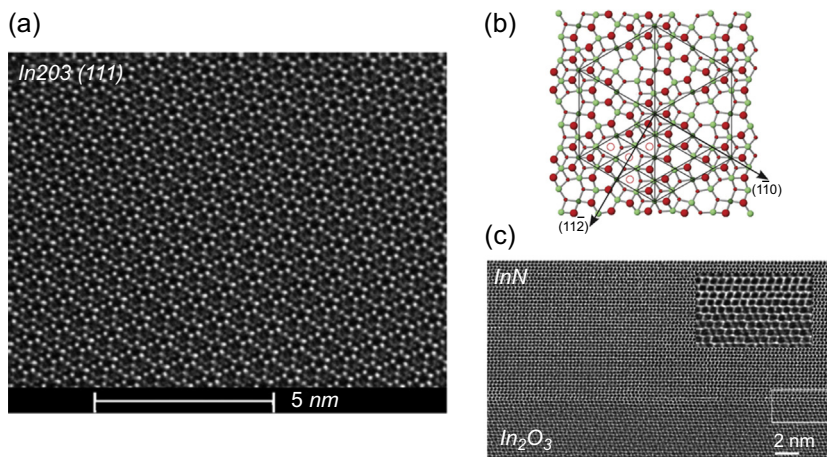


Figure 15.4 (a) High-resolution (HR) TEM image of a melt-grown bulk In_2O_3 single crystal. (b) Top view of the (111) surface formed by a stoichiometric trilayer. Thin solid lines illustrate the 4:1 coincidence lattice of InN (0001) relative to In_2O_3 (111). (c) HR TEM image of the interface between InN and In_2O_3 substrates taken along the $[11\text{--}20]$ direction of InN . The inset is a magnification of the image showing the regular structure of the interface.

(a) Reprinted from Z. Galazka, R. Uecker, K. Irmscher, D. Schulz, D. Klimm, M. Albrecht, M. Pietsch, S. Ganschow, A. Kwasniewski, R. Fornari, Melt growth, characterization and properties of bulk In_2O_3 single crystals, *J. Cryst. Growth* 362 (2013) 349–352, copyright (2013), with permission from Elsevier. (b) and (c) Reprinted from S. Sadofev, Y.J. Cho, O. Brandt, M. Ramsteiner, R. Calarco, H. Riechert, S.C. Erwin, Z. Galazka, M. Korytov, M. Albrecht, R. Uecker, R. Fornari, Growth of wurtzite InN on bulk $\text{In}_2\text{O}_3(111)$ wafers, *Appl. Phys. Lett.* 101 (2012) 172102, copyright (2012), with permission from American Institute of Physics.

single-phase InN by plasma-assisted molecular beam epitaxy [50]. The $\text{InN}/\text{In}_2\text{O}_3$ orientation relationship was confirmed to be $(0001) \parallel (111)$ and $[1100] \parallel [112]$ with an effective mismatch of about 1%, as shown in Fig. 15.4(b). A cross-sectional TEM image indicated the smooth interface (Fig. 15.4(c)), suggesting that In_2O_3 has the potential to be a substrate for the growth of InN .

15.2.3 Epitaxial thin film growth

For practical electronic device applications, thin film technology is also important. Most undoped and doped In_2O_3 are grown in the form of amorphous or polycrystalline thin films or layers by techniques such as spray pyrolysis [51] and hydrolysis [52], sol–gel [53], sputtering [54], electron beam evaporation [55], pulsed laser deposition [56,57], molecular beam epitaxy (MBE) [18,58], metal organic chemical vapor deposition [59,60], and so on. While traditional applications such as TCOs and gas sensors can work with a low material quality, to move to advanced electronic devices such as a channel layer in the transistor, higher-mobility TCOs, high-material quality is mandatory in the film form. To this end, recent efforts on thin film growth by plasma-assisted MBE yielded high-quality material that allows the study of the intrinsic material physics [61,62].

An advantage of heteroepitaxial growth of In_2O_3 is controllability of crystal structure. During epitaxy a crystalline film is aligned to a crystalline substrate. On the cubic substrates, such as InAs, MgO, or $\text{ZrO}_2\text{:Y}$ (YSZ), cubic In_2O_3 grows in a trivial cube-on-cube way. Cubic Y-stabilized ZrO_2 (YSZ) adopts the parent fluorite structure and provides an ideal substrate for growth of high-quality thin films of bcc- In_2O_3 due to a small mismatch of only 1.7%. In_2O_3 thin films with the highest reported electron mobilities of $226 \text{ cm}^2/\text{Vs}$ at room temperature and over $1200 \text{ cm}^2/\text{Vs}$ at 100 K have recently been grown on YSZ substrate by Bierwagen and Speck using oxygen plasma-assisted MBE [63]. In contrast, $\alpha\text{-Al}_2\text{O}_3$ (sapphire) has a rhombohedral crystal structure (space group $R\bar{3}c$) with lattice parameters $a = b = 4.759 \text{ \AA}$ and $c = 12.991 \text{ \AA}$ [64]. This material is widely used for epitaxial growth of ZnO and GaN [65,66], has an unusual epitaxial relationship with cubic In_2O_3 , and forms rhombohedral epitaxial In_2O_3 films. However, be impeded by the large lattice mismatch (above 11%). Cubic In_2O_3 films could form on the $\alpha\text{-Al}_2\text{O}_3$ with a nontrivial epitaxial relation and domain structure. Vogt demonstrated the epitaxial growth of phase-pure cubic In_2O_3 (110) on r-plane sapphire (01 $\bar{1}2$), and achieved a high concentration of Sn or Mg doping of over 10^{20} cm^{-3} [67]. Zhang demonstrated the growth of phase-pure cubic In_2O_3 (111) with rotational domains on rhombohedral $\alpha\text{-Al}_2\text{O}_3$ (0001) [29,61], and a mixture of cubic In_2O_3 (111) and rhombohedral In_2O_3 (00.01) on $\alpha\text{-Al}_2\text{O}_3$ (0001) (Fig. 15.5(a) and (b)). By combining a high-temperature nucleation layer and evolutionary structural selection of the rhombohedral phase during the growth process, Wang realized phase-pure rhombohedral In_2O_3 (0001) on $\alpha\text{-Al}_2\text{O}_3$ (0001) (Fig. 15.5(c)–(e)) [68]. Suzuki also demonstrated the growth of rhombohedral In_2O_3 on $\alpha\text{-Al}_2\text{O}_3$ by inserting an $\alpha\text{-Fe}_2\text{O}_3$ buffer layer, which has an intermediate lattice constant ($a = 5.0351 \text{ \AA}$ [32]), between rhombohedral In_2O_3 and $\alpha\text{-Al}_2\text{O}_3$ [69]. Different crystal phases and their epitaxial relationship to the substrate lead to different crystal properties like electronic or heat transport properties.

15.3 Tailoring of crystal properties

15.3.1 Surface structure and accumulation layer

Using CVT-, melt-, and MBE-grown In_2O_3 crystals, several groups report the fundamental properties of In_2O_3 . Braun et al. measured in-gap defect states of the cleaved {111} surface of In_2O_3 single crystals by scanning tunneling spectroscopy (STS) in the fundamental bandgap, as shown in Fig. 15.6 [48]. The crystal showed the clear dependence of the specific resistivity on the annealing time, suggesting the influence of oxygen treatment. Furthermore, besides the conduction band minimum (CBM) and the valence band maximum (VBM), gap states have been determined with high accuracy in the fundamental bandgap of In_2O_3 in the local density of states (LDOS) spectra by STS. Oxygen vacancies are major defects of In_2O_3 , and defects of minor importance due to oxygen and indium atoms on interstitial lattice sites are identified by combining the density functional theory (DFT) calculations [70]. The defect states at approximately -1 and -1.6 eV are caused by oxygen vacancies (V_{Os}) and doubly occupied oxygen vacancies. The peak at -1.78 eV matches a defect level caused by

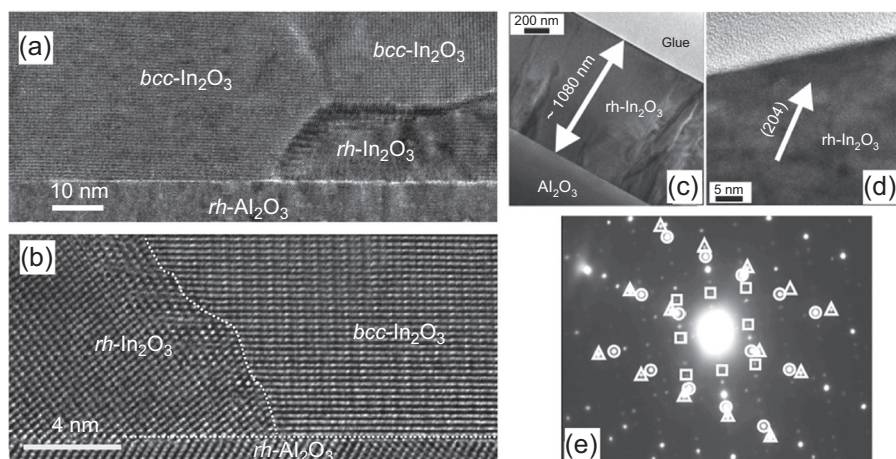


Figure 15.5 (a) Large area TEM image of In_2O_3 layer on Al_2O_3 (0001). Rh- In_2O_3 inclusion close to the interface is surrounded by bcc- In_2O_3 . (b) Expanded HR image shows contrasting structures of rh- and bcc- phases of In_2O_3 . (c) Cross-sectional TEM image shows $\text{In}_2\text{O}_3/\text{Al}_2\text{O}_3$ interface. (d) HRTEM micrograph presents the rh- In_2O_3 structure near the surface area. (e) Selected area electron diffraction (SAED) pattern of $\text{In}_2\text{O}_3/\text{Al}_2\text{O}_3$ interface (triangles: Al_2O_3 , circles: bcc- In_2O_3 , and squares: rh- In_2O_3).

(a) and (b) Reprinted from K.H.L. Zhang, V.K. Lazarov, P.L. Galindo, F.E. Oropeza, D.J. Payne, H.H.-C. Lai, R.G. Egdell, Domain matching epitaxial growth of In_2O_3 thin films on $\alpha\text{-Al}_2\text{O}_3$ (0001), *Cryst. Growth Des.* 12 (2012) 1000–1007, copyright (2012), with permission from American Chemical Society. (c) and (d) Reprinted from C.Y. Wang, Y. Dai, J. Pezoldt, B. Lu, T. Kups, V. Cimalla, O. Ambacher, Phase stabilization and phonon properties of single crystalline rhombohedral indium oxide, *Cryst. Growth Des.* 8 (2008) 1257–1260, copyright (2008), with permission from American Chemical Society.

V_{OS} of lower occupation number. The gap state at -2.37 eV and that around -1.45 eV are probably caused by oxygen on interstitial sites. The states at -2.11 and -1.58 eV could be formed by indium atoms on interstitial sites. The shoulder peaks at approximately -0.01 and -2.78 eV correspond to the CBM and VBM, respectively. The fundamental bandgap of In_2O_3 from the LDOS spectra was determined as 2.78 ± 0.04 eV, which is consistent with the reported bandgap of CVT-grown In_2O_3 crystals obtained by high-resolution angular resolved photoelectron spectroscopy [47].

As mentioned in the introduction, for In_2O_3 the surface accumulation layer is a crucial issue, and may relate to the surface structure and defects. Nagata et al. reported the band diagrams of melt-grown In_2O_3 single crystals estimated from the results of surface-sensitive conventional soft X-ray photoelectron spectroscopy (SXPS; $h\nu = 1486.6$ eV) and bulk-sensitive hard X-ray photoelectron spectroscopy (HAXPS; $h\nu = 5.95$ keV) by combining the simulation of Poisson–Schrödinger solutions, as shown in Fig. 15.7(a) [71]. Within 5 nm of the surface there is a strong downward bending of the bands due to SEAL. At the surface the Fermi level is pinned strongly above the CBM by approximately 1.0 eV regardless of the oxygen annealing

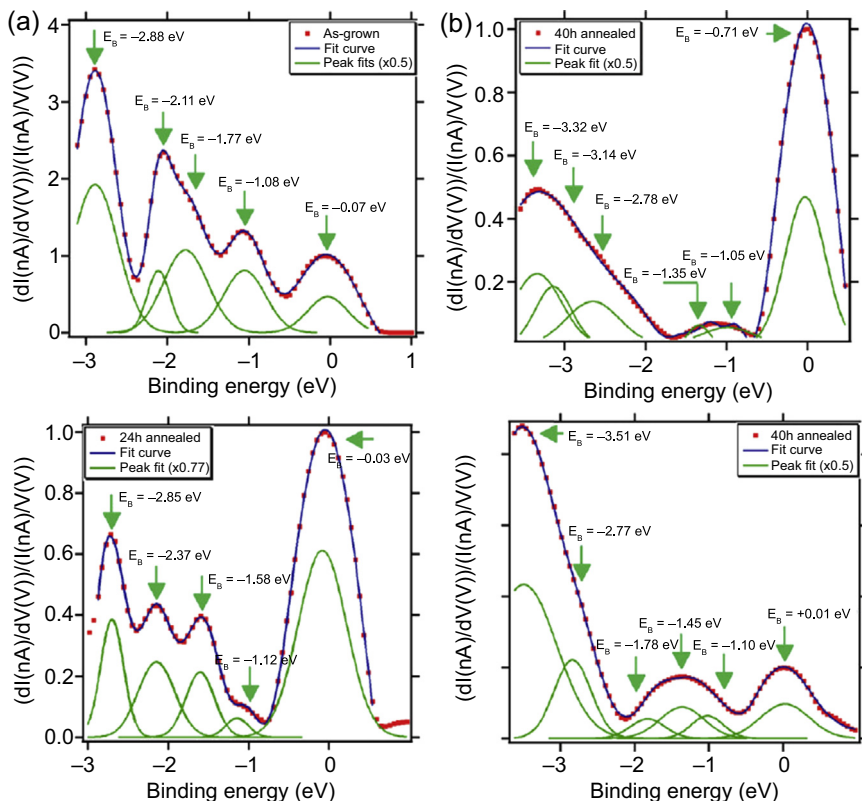


Figure 15.6 (a) LDOS spectra against binding energy measured on as-grown CVT In_2O_3 crystals (top) and those annealed for 24 h in an oxygen flue (bottom) by means of STS. The binding energies of the LDOS maxima have been derived from a least-squares fit (blue line) by Gaussians (green lines) to the experimental curve (red points). (b) LDOS spectra against binding energy measured on In_2O_3 crystals grown from the melt. The STS spectra of two different charges are shown, but both have been annealed for 40 h in air. The binding energies of the LDOS maxima have been derived from a least-squares fit (blue line) by Gaussians (green lines) to the experimental curve (red points).

Reprinted with permission from D. Braun, V. Scherer, C. Janowitz, Z. Galazka, R. Fornari, R. Manzke, In-gap states of In_2O_3 single crystals investigated by scanning tunneling spectroscopy, *Phys. Status Solidi A* (2013) 1–7. Copyright (2013), with permission from WILEY-VCH.

conditions. At the Fermi level (E_F : binding energy = 0 eV) a weak but well-defined feature associated with conduction band states was observed, as shown in Fig. 15.7(b). Conduction band states originate from the electrons in the conduction band below the Fermi level, which is the region below 4 nm. In-gap states attributed to V_O s were observed as similar to the STS results. The bonding states relating to the V_O were also confirmed at the In 3d and O 1s core spectra. However, Scherer et al. observed the absence of SEAL at the surface of the same melt-grown In_2O_3 (111) single crystal, cleaved and investigated in an ultrahigh vacuum condition

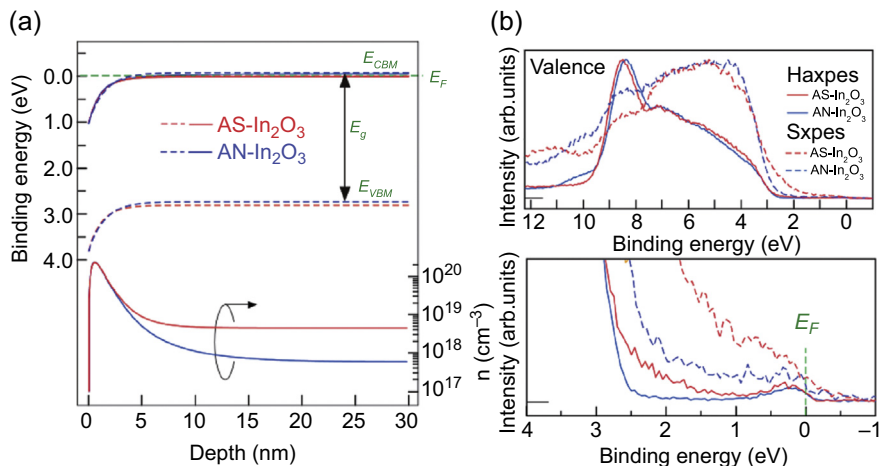


Figure 15.7 (a) The dashed lines at the top show a schematic illustration of band diagrams from the surface (left) to the bulk (right) estimated by SXPES and HAXPES. E_F : Fermi level, E_{CBM} : conduction band minimum, E_{VBM} : VBM, and E_g : bandgap. The solid lines on the top and bottom sides show the diagram of the conduction band and the electron-concentration profile calculated using Poisson–Schrödinger solutions, respectively. (b) Valence band spectra for as grown (AS-) and annealed (AN-) In₂O₃ measured by HAXPES (solid lines) and SXPES (dashed lines). The Fermi level corresponds to 0 eV. The bottom panel is the magnified valence band spectra near E_F .

Reprinted with permission from T. Nagata, O. Bierwagen, Z. Galazka, M. Imura, S. Ueda, H. Yoshikawa, Y. Yamashita, T. Chikyow, Photoelectron spectroscopic study of electronic state and surface structure of In₂O₃ single crystals, Appl. Phys. Express 10 (2017) 011102. Copyright (2017) by the Japan Society of Applied Physics.

($\sim 10^{-9}$ Pa) [72]. Furthermore, in the film SEAL was observed regardless of the crystal orientation [2,11]. Considering both Scherer et al.'s result and HAXPES results, surface structure and adsorption should contribute to form the SEAL. Bierwagen demonstrated SEAL removal by an oxygen plasma treatment, and confirmed an electron depletion at the surface, the absence of the conduction band peak at the Fermi level, and a Schottky contact on an n-type semiconductor [63].

15.3.2 Optical properties

There is still ambiguity in quantitative understanding of the fundamental optical absorption of In₂O₃. Many studies of optical absorption indicate an optical gap of about 3.5–3.8 eV [55,73,74]. Matino et al. showed a direct bandgap of 3.5 ± 0.1 eV and an indirect bandgap of 2.1 ± 0.2 eV of ITO by in-situ room temperature scanning tunneling microscopy observation after an annealing process in ultrahigh vacuum [75]. These results were based on an investigation of thin polycrystalline films. Irmscher pointed out that the steep increase of the absorption coefficient to above 10^5 cm⁻¹ limits the ultraviolet transparency for wavelengths below 335 nm of even

very thin ($<<1\ \mu\text{m}$) In_2O_3 films. The shift of this absorption edge to higher energies with increased tin doping (up to $10^{21}\ \text{cm}^{-3}$), which is applied to obtain high n-type conductivity of the layers, can be explained by the Burstein–Moss effect [3]. Weiher and Ley reported the onset of optical absorption at about 2.6 eV of a single crystalline sample grown from the vapor phase, in addition to the absorption at about 3.7 eV [77]. They suggested that for the indirect band structure, the CBM was at the Γ point of the Brillouin zone and the VBM was away from the Γ point by approximately 1 eV. The absorption edge at 3.7 eV and absorption onset at 2.6 eV were assigned as direct (allowed) transitions at the Γ point and indirect (forbidden) transitions between the VBM and the CBM, respectively. For melt-grown In_2O_3 , Irmscher demonstrated the temperature dependence of optical absorption, and confirmed that the absorption onset at about 2.7 eV corresponded to intrinsic nature, as shown in Fig 15.8(a) [3,28,77]. This lowest-energy bandgap allows us to maintain high transparency at room temperature. The lowest-energy direct transition is dipole forbidden, while the onset of strong absorption due to dipole-allowed direct transitions is at about 3.8 eV [78]. In contrast, theoretical studies resulted in a direct gap at Γ , with two exceptions proposing the VBM away from the Γ but only 50 meV higher than that at the Γ point. A schematic of the band structure is shown in Fig. 15.8(b). By spectroscopic ellipsometry, Feneberg et al. confirmed that the onset of absorption due to dipole-allowed interband transitions was at 3.8 eV for a carrier concentration of below $10^{19}\ \text{cm}^{-3}$ [79]. The onset of absorption shifted to higher absorption onset energies, with increasing electron densities explained by the interplay of Burstein–Moss shift and bandgap renormalization when taking the band nonparabolicity into account. Furthermore, analysis of the plasma frequencies showed that effective electron masses increased from a zero-density mass of $m^* = 0.18m_0$ to $0.4m_0$ at $n = 10^{21}\ \text{cm}^{-3}$ (Fig. 15.8(c)), which is important in understanding the electrical and optical properties of In_2O_3 .

15.4 Theoretical knowledge on In_2O_3

To understand the structural phase stability, electronic structure, and optical properties of In_2O_3 , a first-principle calculation is beneficial. Fundamental understandings of the phase transitions of In_2O_3 relating to the electrical and optical properties are connected to its technological importance in many application fields.

First-principle calculations of In_2O_3 have been performed since the 1990s [80,81]. Several open questions still remain, such as the indirect and direct bandgap, and underestimation of the bandgap relating to the hybridization between In 4d and O 2p states. Albanesi et al. used a tight-binding method to calculate the band structure of In_2O_3 , but did not include the In 4d orbitals in the valence [82]. A discrete variational $X\alpha$ method and a linear combination of atomic orbitals including the In 4d electrons in the valence were reported, and an antibonding contribution near the top of the valence band and an indirect bandgap were observed [78]. DFT calculations by the linear muffin-tin orbital method also demonstrated indirect bandgap, with the VBM at the H point, and found a negative curvature of the valence band near the Γ point [80].

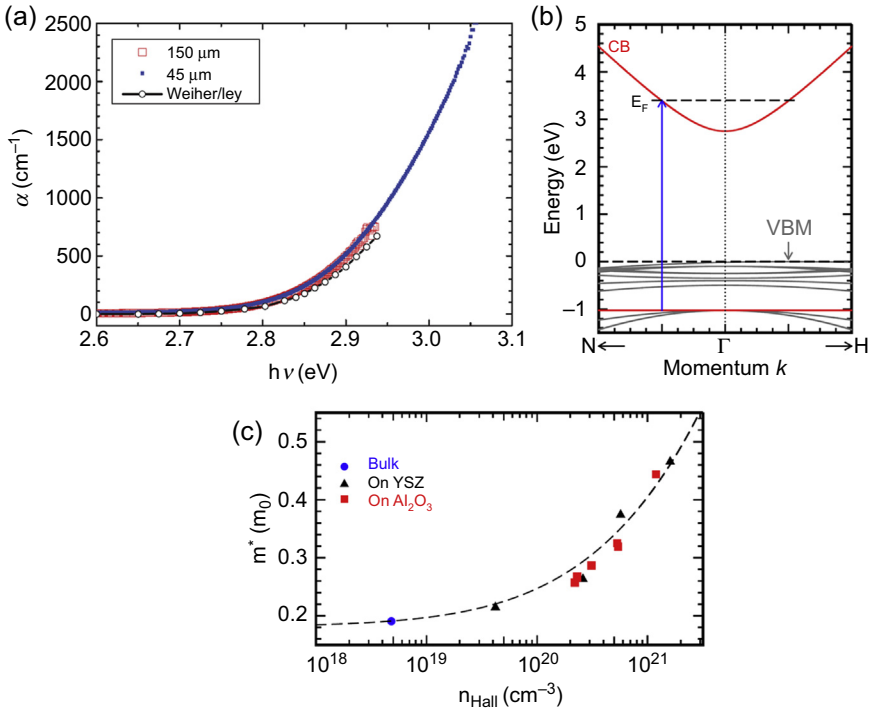


Figure 15.8 (a) Absorption spectral dependence of the absorption coefficient (α) of In_2O_3 at room temperature for two samples with thicknesses of 45 (solid squares) and 150 (open squares) μm . The data represented by a black line connecting open circles is taken from Weiher et al. [77]. (b) The band structure of bixbyite In_2O_3 is calculated by Fuchs and Bechstedt [28] in the vicinity of the Γ point of the Brillouin zone. The band structure is calculated to be indirect with the valence band maximum at $k \neq 0$ on the $-\Gamma$ - H line. The onset of strong absorption (represented by the vertical blue arrow for a selected Fermi energy E_F) originates from transitions from a lower valence band to the conduction band, with its minimum at $k = 0$. These bands are marked in red. Energy values, number, and masses of valence bands are chosen arbitrarily. (c) Determined effective electron masses (m^*) of In_2O_3 as a function of free carrier density (n_{Hall}). The different symbols represent samples grown on different substrates and a bulk crystal. The dashed curve is a nonparabolic model to describe the observed behavior.

(a) Reprinted from T. Minami, Present status of transparent conducting oxide thin-film development for Indium-Tin-Oxide (ITO) substitutes, *Thin Solid Films* 516 (2008) 5822–5828, copyright (2013), with permission from Wiley-VCH. (b) and (c) Reprinted from M. Feneberg, J. Nixdorf, C. Lidig, R. Goldhahn, Many-electron effects on the dielectric function of cubic In_2O_3 : effective electron mass, band nonparabolicity, band gap renormalization, and Burstein-Moss shift, *Phys. Rev. B* 93 (2016) 045203, copyright (2016), with permission from American Physical Society.

However, these results indicated underestimation of the bandgap. Some authors mention that In_2O_3 the description of the metal d levels using the local density or generalized gradient approximation was partly incorrect [83–85]. The energetic position of the In 4d-derived orbitals affects the hybridization of In 4d levels with O 2s and

O 2p levels, affecting the structure near the VBM. In other In compounds, such as InP, the In 4d levels are known to split due to spin-orbit coupling by as much as 0.86 eV [86,87]. If a splitting of this magnitude occurs near the top of the valence band, an indirect band gap could result. Erhart employed the semiempirical local density approximation (LDA) + U and generalized gradient approximation (GGA) + U schemes [83] in the version by Dudarev [88], incorporating self-interaction corrections into the LDA and GGA functionals. The self-interaction parameter $U-J$ was varied between 0 and 9 eV. The results obtained are consistent with available spectroscopic data [83,89–91], as shown in Fig. 15.9.

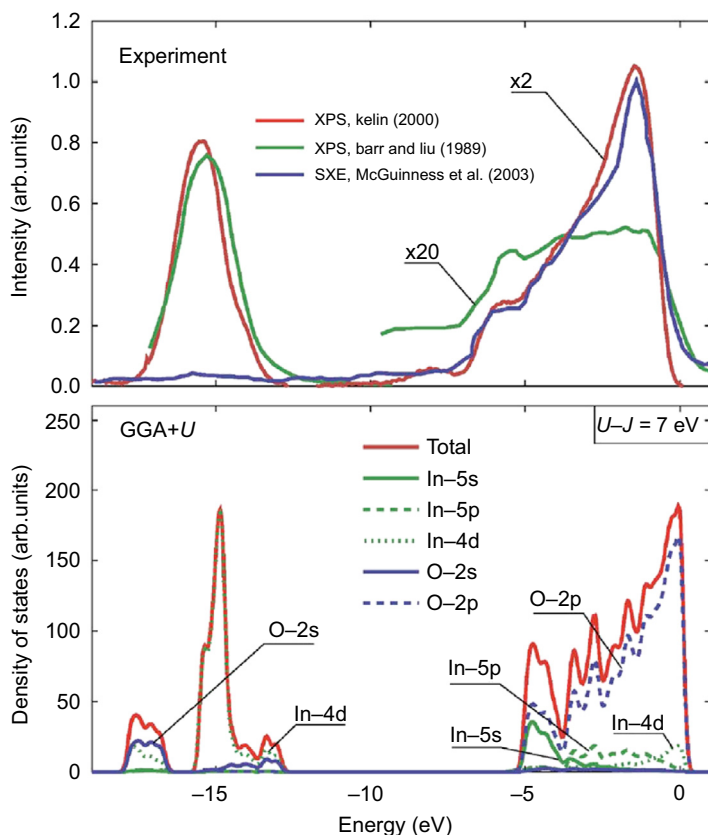


Figure 15.9 Total and partial densities of states from GGA + U calculations using $\bar{U} - \bar{J} = 7$ eV. The results of X-ray photoelectron spectroscopy [94,95] and soft X-ray emission [96] spectroscopy measurements are shown for comparison. For better visualization the calculated density of states was broadened using a Gaussian filter with 0.1 eV and multiplied by a factor of five for energies larger than -8 eV.

Reprinted with permission from P. Erhart, A. Klein, R.G. Egdell, K. Albe, Band structure of indium oxide: indirect versus direct band gap, *Phys. Rev. B*, 75 (2007) 153205. Copyright (2007) by the American Physical Society.

The self-interaction in the $4d$ shell is corrected for by taking into account an empirical Coulomb interaction parameter U . Nevertheless, the energy gaps remain too small, as the excitation aspect is not included in the electronic structure calculation. The parameter U is found to influence the position of VBM in k space, and hence the relation between the direct and indirect bandgaps. Fuchs considers the influence of the actual crystallographic structure of In_2O_3 on the electronic bands. Concerning the crystallographic structure effect, Karazhanov et al. reported on structural phase stability, electronic structure, optical properties, and high-pressure behavior of In_2O_3 ; In_2O_3 was found to convert from bixbyite to corundum at a high pressure of around 3.8 GPa [27]. Calculations within local density and generalized gradient approximations indicated that the corundum-type In_2O_3 was an indirect bandgap semiconductor, while the bixbyite-type In_2O_3 was direct bandgap but remains within the framework of DFT–LDA and GGA. In contrast, Fuchs and Bechstedt studied the electronic structure on the basis of the hybrid HSE03 XC functional [28]. The structural phase stability is similar to the results found by Karazhanov. Both structures show similar electronic properties, especially densities of states. The bandgap of the bixbyite-type In_2O_3 is slightly indirect or direct. The calculated direct quasiparticle gaps of the bixbyite and corundum types amount to 3.1 and 3.3 eV, respectively. The lowest indirect gaps of the bixbyite and corundum types are 2.61 and 2.45 eV, respectively. Furthermore, the Burstein–Moss shift and Fermi level position and average effective mass as a function of the free electron density were calculated, and were similar to the experimental results (Fig. 15.8(a)). The corundum-type In_2O_3 is almost same as the bixbyite-type In_2O_3 .

15.5 Doping issues and reduction of defect density

15.5.1 Unintentionally doped In_2O_3

The first principle suggested the origin donors in unintentionally doped In_2O_3 as V_{O} and hydrogen. Ágoston et al. demonstrated the existence of doubly positive (V_{O}^{2+}) and neutral (V_{O}^0) defects in In_2O_3 by using the LDA and GGA functions, as shown in Fig. 15.10(a) [93]. The V_{O} is a shallow donor with a low formation energy at reducing conditions, suggesting that abundant V_{O} s are the cause of the intrinsic n-type behavior. Furthermore, Tang et al. suggested that an indium interstitial (In_i) or a tin dopant (Sn : $\text{In}-V_{\text{O}}$) induces a shallow donor [94]. The coupling between these shallow donor levels and a deep donor level corresponding to a V_{O} leads to a significant reduction in their formation energies, meaning the formation of defect pairs. Annealing in oxygen also decreased the electron concentrations of bulk single crystal or high-quality thin films [34]. In contrast, Limpijumnong et al. find that both interstitial hydrogen (H_i) and substitutional hydrogen (H_{O}) act as shallow donors by LDA + U calculations [95]. The anion antibonding sites are the preferred site for H_i^+ owing to the long In–O bond. The H_i^+ site is lower in energy than the other metastable sites. The H substitution on the O site is also exclusively a donor. Experimentally, Koida et al. demonstrated

H-doped In_2O_3 films by radiofrequency magnetron sputtering [96]. H composition controlled by varying water vapor pressure during the growth showed correlation with electrical properties [97]. The 1.9–6.3 at% H-contained films showed as high as $98\text{--}130\text{ cm}^2/\text{Vs}$ at carrier concentration of $1.8 \times 10^{20}\text{ cm}^{-3}$. Furthermore, King et al. performed muon spin rotation measurements to investigate the electrical behavior of hydrogen in In_2O_3 [98]. By probing the electrical behavior of muonium in In_2O_3 , a shallow-donor center was observed with an activation energy of 47.6 meV. Stavola et al. used infrared (IR) spectroscopy to investigate the properties of H in In_2O_3 single crystals [99]. The majority of the free-carrier absorption was produced by the interstitial H (H_i) defect only. The IR spectrum corresponding to the defect with H trapped by an oxygen vacancy (H_o) was not confirmed.

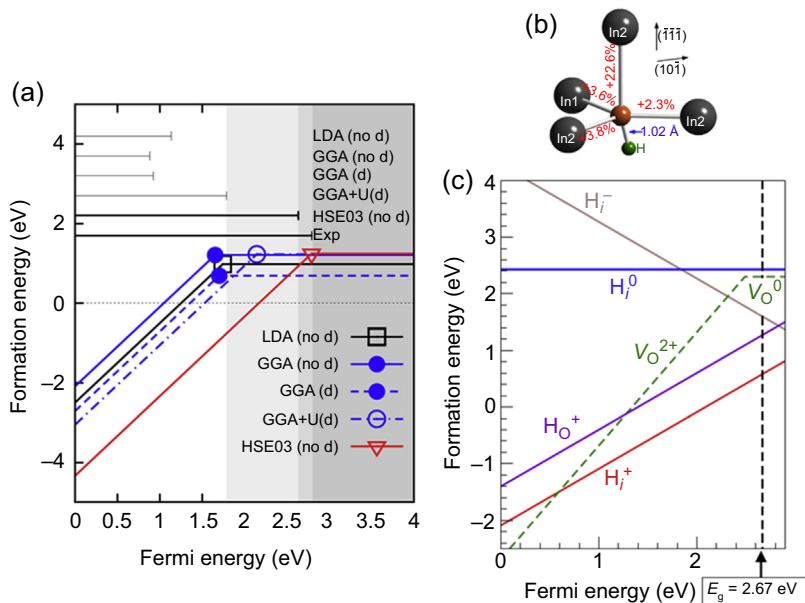


Figure 15.10 (a) Formation energies of V_O s in In_2O_3 at reducing conditions. The lines with positive and zero slopes refer to V_O^{2+} and V_O^0 , respectively. V_O^{+} is unstable. The horizontal bar on the top shows the calculated and experimental bandgaps. The LDA/GGA + U, HSE06/PBE0, and experimental bandgaps are denoted by shaded areas. (b) Schematic illustration of H defects in In_2O_3 (H_i^+ at the $\text{AB}_{\text{O}1}$ site). (c) Calculated formation energies of hydrogen defects and V_O s in In_2O_3 as a function of Fermi energy.

(a) Reprinted from P. Ágoston, K. Albe, R.M. Nieminen, M.J. Puska, Intrinsic n-type behavior in transparent conducting oxides: a comparative hybrid-functional study of In_2O_3 , SnO_2 , and ZnO , *Phys. Rev. Lett.* 103 (2009) 245501, copyright (2009), with permission from the American Physical Society. (b) and (c) Reprinted from S. Limpijumnong, P. Reunchan, A. Janotti, C.G. Van de Walle, Hydrogen doping in indium oxide: an ab initio study, *Phys. Rev. B* 80 (2009) 193202, copyright (2009), with permission from the American Physical Society.

15.5.2 Intentionally doped In_2O_3

For n-type doping, Sn has been regarded as the only useful dopant for In_2O_3 , which is supported by the first-principle calculation. There is much experiment research using the various n-type dopants. High-mobility and near-IR-transparent In_2O_3 thin films have been reported for several doping metals, such as Mo [100,101], Ti [6], W [102], and Zr [103], which showed high carrier mobility of around $80 \text{ cm}^2/\text{Vs}$ with carrier density larger than 10^{20} cm^{-3} . However, both the best doping elements and the origins of high mobility are still unclear. The electrical properties of polycrystalline film grown on glass at a low temperature depend on the growth method and/or conditions. There are many reasons for electron carrier generation, such as V_{O} , interstitial metals, and extrinsic dopants. These mechanisms occur simultaneously. To simplify the effects of various dopants on the electrical properties, single crystals or epilayers are beneficial. Bierwagen made a systematic investigation of Sn doping in the epitaxial In_2O_3 films grown by plasma-assisted MBE with small numbers of intrinsic donors [104]. The electron concentration increased and resistivity decreased with increasing Sn concentration, as shown in Fig. 15.11(a). These properties were improved by post-deposition annealing in a vacuum to remove compensating acceptors such as oxygen interstitials.

For p-type doping, unintentional p-type conductivity has not been observed in single crystalline In_2O_3 , as acceptor-like intrinsic point defects like indium vacancy V_{In} and oxygen interstitial O_i can act as compensating centers. Agoston et al. also suggested that the low formation energies predicted by hybrid-functional calculations are low for the oxygen-rich growing conditions [93]. The V_{O} formation energies even become negative for the electron chemical potential near the VBM, indicating that p-type doping is impossible for these materials close to the thermodynamic equilibrium. However, acceptor doping gives a chance of obtaining high-quality p-type In_2O_3 or semiinsulating material. Weiher demonstrated one order of magnitude lower room-temperature conductivity of a Zn-doped sample compared to unintentionally doped samples using bulk single crystals [105], and the same qualitative effect was shown by de Wit with Ca-doped polycrystalline bulk samples [106]. Bierwagen prepared highly Mg-doped MBE-grown In_2O_3 and found the dopant concentration dependence of the resistivity after annealing in oxygen [107], as shown in Fig. 15.11(b). The highest Mg-doped sample, with a dopant concentration of $6 \times 10^{20} \text{ cm}^{-3}$, showed a semiinsulating property with a film resistivity of above 10^5 cm , although p-type conductivity was not observed. Other authors investigated the compensating vacancy defects (V_{In} , V_{O}) by positron annihilation spectroscopy in Sn-donor and Mg-acceptor doped In_2O_3 thin films [108]. In both types of oxygen-annealed films, acceptor type V_{In} was detected. The concentration of the V_{In} in the Sn-donor-doped sample was higher than that in Mg-acceptor-doped samples, suggesting that the interstitial oxygen O_i may be the main compensating acceptor. However, isolated V_{O} was not observed. The reason for the overcompensation of the Mg by the donor is still unclear.

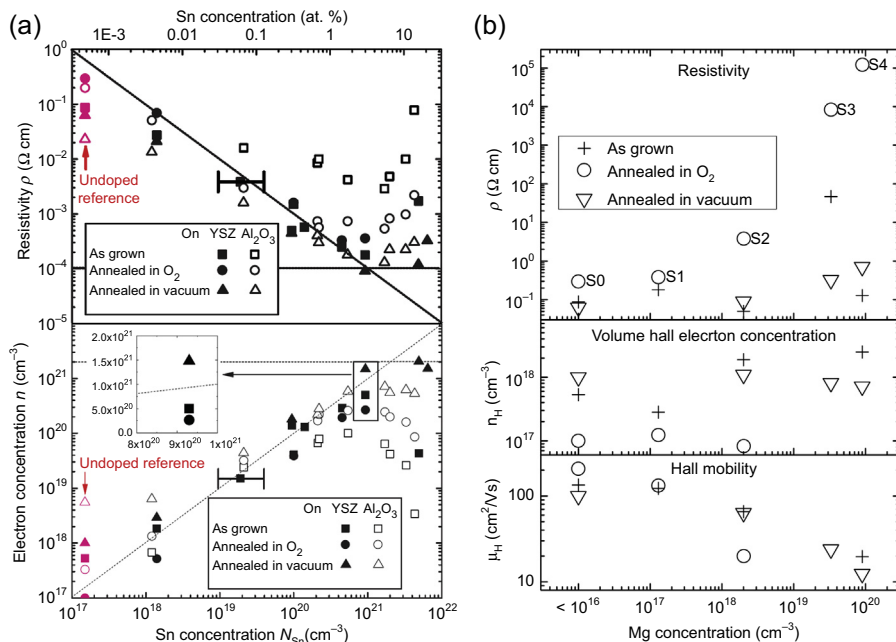


Figure 15.11 Volume Hall electron concentration (n) and resistivity (ρ) as function of Sn-concentration (N_{Sn}) for as-grown and postgrowth-treated samples (annealed in oxygen, annealed in vacuum). The colored data points at the lowest Sn concentration correspond to an undoped reference film. The inset highlights the substantial impact of postgrowth annealing on electron concentration for extremely high Sn concentrations. The diagonal dashed line corresponds to $n = N_{\text{Sn}}$; the horizontal line denotes our empirical electron concentration (*dashed line*) and resistivity (*solid line*) limits. The horizontal error bar indicates the uncertainty of the secondary ion mass spectrometry (SIMS) measurement. (b) Film resistivity ρ , Hall electron concentration (n_H), and Hall mobility (μ_H) of Mg-doped films as a function of Mg concentration and annealing conditions. The data points at an Mg concentration of $< 10^{16} \text{ cm}^{-3}$ were taken with the unintentionally doped reference sample. For samples with resistivity above $10 \text{ } \Omega \text{ cm}$ only the resistivity could be reliably determined and no Hall data is given. (a) Reprinted from O. Bierwagen, J.S. Speck, Plasma-assisted molecular beam epitaxy of Sn-doped In_2O_3 : Sn incorporation, structural changes, doping limits, and compensation, *Phys. Status Solidi A*, 211 (2014) 48–53, copyright (2013), with permission from WILEY-VCH. (b) Reprinted from O. Bierwagen, J.S. Speck, Mg acceptor doping of In_2O_3 and overcompensation by oxygen vacancies, *Appl. Phys. Lett.* 101 (2012) 102107, copyright (2012), with permission from American Institute of Physics.

15.6 Summary

In earlier years In_2O_3 -based oxides drew attention as TCOs for transparent electrodes in their amorphous or polycrystalline thin film form, with a lack of understanding of their intrinsic physical properties. After 2000 the progress of single crystal and

epitaxial growth technologies has accelerated research concerning the intrinsic physical properties of In_2O_3 by combining the modern first-principle calculation and high-resolution analysis technologies. The indirect bandgap is approximately 2.7 eV; the effective electron mass is around $0.2m_0$; the high-quality epitaxial film achieved high Hall mobilities of over $200\text{ cm}^2/\text{Vs}$; and the high concentration of n-type doping has been demonstrated below a resistivity of $10^{-4}\ \Omega\text{cm}$. Although there are still some open issues, such as p-type doping, SEAL formation, and the actual origin of intrinsic donors (either as V_{Os} or hydrogen vacancies), the new knowledge is useful for electronic device applications. For use of In_2O_3 in advanced electronic device applications, key technologies are the doping for spintronics [22], nanostructured crystal growth, and alloying. Single crystalline nanostructured In_2O_3 has been reported [109]. In other compound semiconductor materials high-quality single nanocrystals have been applied to field-effect transistors and optical devices with a high affinity to Si-based nanoelectronic devices [110,111]. Concerning alloying, Ga_2O_3 has recently attracted attention as a potential material for power devices [112], but there are issues such as carrier control, bandgap engineering, and crystal structure control. To overcome these issues, an Al–I–GaO_x system should have the same potential for physical property control as the Al–In–GaN system.

References

- [1] J.E. Medvedeva, C.L. Hettiarachchi, Tuning the properties of complex transparent conducting oxides: role of crystal symmetry, chemical composition, and carrier generation, *Phys. Rev. B* 81 (2010) 125116J.
- [2] P.D.C. King, T.D. Veal, F. Fuchs, ChY. Wang, D.J. Payne, A. Bourlange, H. Zhang, G.R. Bell, V. Cimalla, O. Ambacher, R.G. Egdell, F. Bechstedt, C.F. McConville, Band gap, electronic structure, and surface electron accumulation of cubic and rhombohedral In_2O_3 , *Phys. Rev. B* 79 (2009) 205211.
- [3] K. Irmscher, M. Naumann, M. Pietsch, Z. Galazka, R. Uecker, T. Schulz, R. Schewski, M. Albrecht, R. Fornari, On the nature and temperature dependence of the fundamental band gap of In_2O_3 , *Phys. Status Solidi A* 211 (2014) 54.
- [4] T. Minami, Present status of transparent conducting oxide thin-film development for Indium-Tin-Oxide (ITO) substitutes, *Thin Solid Films* 516 (2008) 5822–5828.
- [5] Y. Meng, X. Yang, H. Chen, J. Shen, Y. Jiang, Z. Zhang, Z. Hua, A new transparent conductive thin film $\text{In}_2\text{O}_3\text{:Mo}$, *Thin Solid Films* 394 (2001) 219.
- [6] M.F.A.M. van Hest, M.S. Dabney, J.D. Perkins, D.S. Ginley, M.P. Taylor, Titanium-doped indium oxide: a high-mobility transparent conductor, *Appl. Phys. Lett.* 87 (2005) 032111.
- [7] H. Ohta, M. Orita, M. Hirano, H. Tanji, H. Kawazoe, H. Hosono, Highly electrically conductive indium–tin–oxide thin films epitaxially grown on yttria-stabilized zirconia (100) by pulsed-laser deposition, *Appl. Phys. Lett.* 76 (2000) 2740.
- [8] J. Rombach, A. Papadogianni, M. Mischo, V. Cimalla, L. Kirste, O. Ambacher, T. Berthold, S. Krischok, M. Himmerlich, S. Selve, O. Bierwagen, The role of surface electron accumulation and bulk doping for gas-sensing explored with single-crystalline In_2O_3 thin films (2016), *Sens. Actuators B Chem.* 236 (2016) 909–916.

- [9] H. von Wenckstern, D. Splith, F. Schmidt, M. Grundmann, O. Bierwagen, J.S. Speck, Schottky contacts to In_2O_3 , *APL Mater.* 2 (2014) 046104.
- [10] H. von Wenckstern, D. Splith, S. Lanzinger, F. Schmidt, S. Müller, P. Schlupp, R. Karsthof, M. Grundmann, pn-Heterojunction Diodes with n-Type In_2O_3 , *Adv. Electron. Mater.* 1 (2015) 1400026.
- [11] O. Bierwagen, J.S. Speck, T. Nagata, T. Chikyow, Y. Yamashita, H. Yoshikawa, K. Kobayashi, Depletion of the In_2O_3 (001) and (111) surface electron accumulation by an oxygen plasma surface treatment, *Appl. Phys. Lett.* 98 (2011) 172101.
- [12] T. Nagata, O. Bierwagen, M.E. White, M.-Y. Tsai, Y. Yamashita, H. Yoshikawa, N. Ohashi, K. Kobayashi, T. Chikyow, J.S. Speck, XPS study of Sb-/In-doping and surface pinning effects on the Fermi level in SnO_2 (101) thin films, *Appl. Phys. Lett.* 98 (2011) 232107.
- [13] M.W. Allen, C.H. Swartz, T.H. Myers, T.D. Veal, C.F. McConville, S.M. Durbin, Bulk transport measurements in ZnO: the effect of surface electron layers, *Phys. Rev. B* 81 (2010) 075211.
- [14] R. Schifano, E.V. Monakhov, U. Grossner, B.G. Svensson, Electrical characteristics of palladium Schottky contacts to hydrogen peroxide treated hydrothermally grown ZnO, *Appl. Phys. Lett.* 91 (2007) 193507.
- [15] L.R. Bailey, T.D. Veal, C.E. Kendrick, S.M. Durbin, C.F. McConville, Sulfur passivation of InN surface electron accumulation, *Appl. Phys. Lett.* 95 (2009) 192111.
- [16] K.H.L. Zhang, R.G. Egddell, F. Offi, S. Iacobucci, L. Petaccia, S. Gorovikov, P.D.C. King, Microscopic origin of electron accumulation in In_2O_3 , *Phys. Rev. Lett.* 110 (2013) 056803.
- [17] M. Nazarzahdemoafi, F. Titze, S. Machulik, C. Janowitz, Z. Galazka, R. Manzke, M. Mulazzi, Comparative study of the electronic structures of the in and Sn/ In_2O_3 (111) interfaces, *Phys. Rev. B* 93 (2016) 081303 (R).
- [18] K. Nomura, H. Ohta, K. Ueda, T. Kamiya, M. Hirano, H. Hosono, Thin-film transistor fabricated in single-crystalline transparent oxide semiconductor, *Science* 300 (2003) 1269.
- [19] Y.H. Hwang, J.H. Jeon, K.J. Seo, B.S. Bae, Solution-processed, high performance aluminum indium oxide thin-film transistors fabricated at low temperature, *Electrochem. Solid State Lett.* 12 (2009) H336.
- [20] P.K. Nayak, J.V. Pinto, G. Goncalves, R. Martins, E. Fortunato, Environmental, optical, and electrical stability study of solution-processed zinc–tin–oxide thin-film transistors, *J. Disp. Technol.* 7 (2011) 640.
- [21] H. Yanagi, T. Hase, S. Ibuki, K. Ueda, H. Hosono, Bipolarity in electrical conduction of transparent oxide semiconductor CuInO_2 with delafossite structure, *Appl. Phys. Lett.* 78 (2001) 1583.
- [22] J. Philip, A. Punnoose, B.I. Kim, K.M. Reddy, S. Layne, J.O. Holmes, B. Satpati, P.R. Leclair, T.S. Santos, J.S. Moodera, Carrier-controlled ferromagnetism in transparent oxide semiconductors, *Nat. Mater.* 5 (2006) 298.
- [23] L. Brewer, Thermodynamic properties of the oxides and their vaporization processes, *Chem. Rev.* 52 (1953) 1.
- [24] R.P. Burns, G. Demaria, J. Drowart, M.G. Inghram, Mass spectrometric investigation of the vaporization of In_2O_3 , *J. Chem. Phys.* 38 (1963) 1035.
- [25] J.-N. Valderrama, K.T. Jacob, Vapor pressure and dissociation energy of (In_2O), *Thermochim. Acta* 21 (1977) 215–224.
- [26] N.M. Lakin, G. van den Hoek, I.R. Beattie, J.M. Brown, The identification of In_2O in the gas phase by high resolution electronic spectroscopy, *J. Chem. Phys.* 107 (1997) 4439.

- [27] M. Marezio, Refinement of the crystal structure of In_2O_3 at two wavelengths, *Acta Crystallogr.* 20 (1966) 723.
- [28] F. Fuchs, F. Bechstedt, Indium-oxide polymorphs from first principles: quasiparticle electronic states, *Phys. Rev. B* 77 (2008) 155107.
- [29] K.H.L. Zhang, V.K. Lazarov, P.L. Galindo, F.E. Oropeza, D.J. Payne, H.H.-C. Lai, R.G. Egdell, Domain matching epitaxial growth of In_2O_3 thin films on $\alpha\text{-Al}_2\text{O}_3(0001)$, *Cryst. Growth Des.* 12 (2012) 1000–1007.
- [30] R.D. Shannon, New high pressure phases having the corundum structure, *Solid State Commun.* 4 (1966) 629.
- [31] A.F. Reid, A.E. Ringwood, High-pressure scandium oxide and its place in the molar volume relationships of dense structures of M_2X_3 and ABX_3 type, *J. Geophys. Res.* 74 (1969) 3238.
- [32] C.T. Prewitt, R.D. Shannon, D.B. Rogers, A.W. Sleight, C rare earth oxide-corundum transition and crystal chemistry of oxides having the corundum structure, *Inorg. Chem.* 8 (1969) 1985.
- [33] http://www.crct.polymtl.ca/factsage/index_m.php.
- [34] Z. Galazka, R. Uecker, K. Irmscher, D. Schulz, D. Klimm, M. Albrecht, M. Pietsch, S. Ganschow, A. Kwasniewski, R. Fornari, Melt growth, characterization and properties of bulk In_2O_3 single crystals, *J. Cryst. Growth* 362 (2013) 349–352.
- [35] A.B. Chase, Growth of $\beta\text{-Ga}_2\text{O}_3$ by the Verneuil technique, *J. Am. Ceram. Soc.* 47 (1964) 470.
- [36] M.R. Lorenz, J.F. Woods, R.J. Gambino, Some electrical properties of the semiconductor $\beta\text{-Ga}_2\text{O}_3$, *J. Phys. Chem. Solids* 28 (1967) 403.
- [37] T. Harwig, J. Schoonman, Electrical properties of $\beta\text{-Ga}_2\text{O}_3$ single crystals. II, *J. Solid State Chem.* 23 (1978) 205.
- [38] N. Ueda, H. Hosono, R. Waseda, H. Kawazoe, Synthesis and control of conductivity of ultraviolet transmitting $\beta\text{-Ga}_2\text{O}_3$ single crystals, *Appl. Phys. Lett.* 70 (1997) 3561.
- [39] Y. Tamm, J.M. Ko, A. Yoshikawa, T. Fukuda, Floating zone growth of $\beta\text{-Ga}_2\text{O}_3$: a new window material for optoelectronic device applications, *Sol. Energy Mater. Sol. Cells* 66 (2001) 369.
- [40] E.G. Villora, K. Shimamura, Y. Yoshikawa, K. Aoki, N. Ichinose, Large-size $\beta\text{-Ga}_2\text{O}_3$ single crystals and wafers, *J. Cryst. Growth* 270 (2004) 420.
- [41] Y. Tamm, P. Reiche, D. Klimm, T. Fukuda, Czochralski grown Ga_2O_3 crystals, *J. Cryst. Growth* 220 (2000) 510.
- [42] Z. Galazka, R. Uecker, K. Irmscher, M. Albrecht, D. Klimm, M. Pietsch, M. Brutzam, R. Bertram, S. Ganschow, R. Fornari, Czochralski growth and characterization of $\beta\text{-Ga}_2\text{O}_3$ single crystals, *Cryst. Res. Technol.* 45 (2010) 1229.
- [43] R. Nitsche, Crystal chemistry, growth and properties of multi-cation chalcogenides, *J. Phys. Colloq.* 36 (1975) C3–C9.
- [44] H. Schäfer, Nachweis und anwendung von gaskomplexen beim chemischen transport, *Z. Anorg. Allg. Chem.* 403 (1974) 116.
- [45] J.J.H.W. De Wit, Preparation of In_2O_3 single-crystals via chemical transport reaction, *J. Cryst. Growth* 12 (1972) 183.
- [46] M. Jozefowicz, W. Piekarczyk, Preparation of In_2O_3 single crystals by chemical vapour transport method, *Mater. Res. Bull.* 22 (1987) 775.
- [47] V. Scherer, C. Janowitz, A. Krapf, H. Dwelk, D. Braun, R. Manzke, Transport and angular resolved photoemission measurements of the electronic properties of In_2O_3 bulk single crystals, *Appl. Phys. Lett.* 100 (2012) 212108.

- [48] D. Braun, V. Scherer, C. Janowitz, Z. Galazka, R. Fornari, R. Manzke, In-gap states of In_2O_3 single crystals investigated by scanning tunneling spectroscopy, *Phys. Status Solidi A* (2013) 1–7.
- [49] Z. Galazka, R. Uecker, R. Fornari, A novel crystal growth technique from the melt: levitation-Assisted Self-Seeding Crystal Growth Method, *J. Cryst. Growth* 388 (2014) 61–69.
- [50] S. Sadofev, Y.J. Cho, O. Brandt, M. Ramsteiner, R. Calarco, H. Riechert, S.C. Erwin, K. Galazka, M. Korytov, M. Albrecht, R. Uecker, R. Fornari, Growth of wurtzite InN on bulk $\text{In}_2\text{O}_3(111)$ wafers, *Appl. Phys. Lett.* 101 (2012) 172102.
- [51] J.J. Prince, S. Ramamurthy, B. Subramanian, C. Sanjeeviraja, M. Jayachandran, Spray pyrolysis growth and material properties of In_2O_3 films, *J. Cryst. Growth* 240 (2002) 142–151.
- [52] T. Yan, X. Wang, J. Long, H. Lin, R. Yuan, W. Dai, Z. Li, X. Fu, Controlled preparation of In_2O_3 , InOOH and $\text{In}(\text{OH})_3$ via a one-pot aqueous solvothermal route, *N. J. Chem.* 32 (2008) 1843–1846.
- [53] A. Gurlo, M. Ivanovskaya, A. Pfau, U. Weimar, W. Göpel, Sol-gel prepared In_2O_3 thin films, *Thin Solid Films* 307 (1997) 288–293.
- [54] H.K. Müller, Electrical and optical properties of sputtered In_2O_3 films, *Phys. Status Solidi* 27 (1968) 723.
- [55] I. Hamberg, C.G. Granqvist, Evaporated Sn-doped In_2O_3 films: basic optical properties and applications to energy-efficient windows, *J. Appl. Phys.* 60 (1986) R123.
- [56] E.J. Tarsa, J.H. English, J.S. Speck, Pulsed laser deposition of oriented In_2O_3 on (001) InAs , MgO , and yttria-stabilized zirconia, *Appl. Phys. Lett.* 62 (1993) 2332.
- [57] H. Ohta, M. Orita, M. Hirano, H. Hosono, Surface morphology and crystal quality of low resistive indium tin oxide grown on yttria-stabilized zirconia, *J. Appl. Phys.* 91 (2002) 3547.
- [58] N. Taga, M. Maekawa, Y. Shigesato, I. Yasui, M. Kamei, T.E. Haynes, Deposition of heteroepitaxial In_2O_3 thin films by molecular beam epitaxy, *Jpn. J. Appl. Phys.* 37 (1998) 6524–6529.
- [59] C.Y. Wang, V. Cimalla, H. Romanus, T. Kups, G. Ecke, T. Stauden, M. Ali, V. Lebedev, J. Pezoldt, O. Ambacher, Phase selective growth and properties of rhombohedral and cubic indium oxide, *Appl. Phys. Lett.* 89 (2006) 011904.
- [60] F. Yang, J. Ma, X.J. Feng, L.Y. Kong, Structural and photoluminescence properties of single-crystalline In_2O_3 films grown by metal organic vapor deposition, *J. Cryst. Growth* 310 (2008) 4054–4057.
- [61] Z. Mei, Y. Wang, X. Du, Z. Zeng, M. Ying, H. Zheng, J. Jia, Q. Xue, Z. Zhang, Growth of In_2O_3 single-crystalline film on sapphire (0001) substrate by molecular beam epitaxy, *J. Cryst. Growth* 289 (2006) 686.
- [62] E.H. Morales, Y. He, M. Vinnichenko, B. Delley, U. Diebold, Surface structure of Sn-doped In_2O_3 (111) thin films by STM, *N. J. Phys.* 10 (2008) 125030.
- [63] O. Bierwagen, J.S. Speck, High electron mobility In_2O_3 (001) and (111) thin films with nondegenerate electron concentration, *Appl. Phys. Lett.* 97 (2010) 072103.
- [64] W.E. Lee, K.P.D. Lagerlof, Structural and electron diffraction data for sapphire ($\alpha\text{-Al}_2\text{O}_3$), *J. Electron. Microsc. Tech.* 2 (1985) 247–258.
- [65] Y.F. Chen, H.J. Ko, S.K. Hong, T. Yao, Layer-by-layer growth of ZnO epilayer on $\text{Al}_2\text{O}_3(0001)$ by using a MgO buffer layer, *Appl. Phys. Lett.* 76 (2000) 559.
- [66] S. Strite, H. Morkoc, GaN , AlN , and InN : a review, *J. Vac. Sci. Technol. B* 10 (1992) 1237.

- [67] P. Vogt, A. Trampert, M. Ramsteiner, O. Bierwagen, Domain matching epitaxy of cubic In_2O_3 on r-plane sapphire, *Phys. Status Solidi A* 212 (2015) 1433–1439.
- [68] C.Y. Wang, Y. Dai, J. Pezoldt, B. Lu, Th Kups, V. Cimalla, O. Ambacher, Phase stabilization and phonon properties of single crystalline rhombohedral indium oxide, *Cryst. Growth Des.* 8 (2008) 1257–1260.
- [69] N. Suzuki, K. Kaneko, S. Fujita, Growth of corundum-structured In_2O_3 thin films on sapphire substrates with Fe_2O_3 buffer layers, *J. Cryst. Growth* 364 (2013) 30–33.
- [70] P. Ágoston, P. Erhart, A. Klein, K. Albe, Geometry, electronic structure and thermodynamic stability of intrinsic point defects in indium oxide, *J. Phys. Condens. Matter* 21 (2009) 455801.
- [71] T. Nagata, O. Bierwagen, Z. Galazka, M. Imura, S. Ueda, H. Yoshikawa, Y. Yamashita, T. Chikyow, Photoelectron spectroscopic study of electronic state and surface structure of In_2O_3 single crystals, *Appl. Phys. Express* 10 (2017) 011102.
- [72] V. Scherer, C. Janowitz, Z. Galazka, M. Nazarzadehmoafi, R. Manzke, Polaron character of the near- E_F band of cleaved $\text{In}_2\text{O}_3(111)$ single crystals, *Europhys. Lett.* 113 (2016) 26003.
- [73] Z.M. Jarzebski, Preparation and physical properties of transparent conducting oxide films, *Phys. Status Solidi A* 71 (1982) 13.
- [74] J. Szczyrbowski, A. Dietrich, H. Hoffmann, Optical and electrical properties of RF-sputtered indium–tin oxide films, *Phys. Status Solidi A* 78 (1983) 243.
- [75] F. Matino, L. Persano, V. Arima, D. Pisignano, R.I.R. Blyth, R. Cingolani, R. Rinaldi, Electronic structure of indium–tin–oxide films fabricated by reactive electron-beam deposition, *Phys. Rev. B* 72 (2005) 085437.
- [76] I. Hamberg, C.G. Granqvist, K.-F. Berggren, B.E. Sernelius, L. Engström, Band-gap widening in heavily Sn-doped In_2O_3 , *Phys. Rev. B* 30 (1984) 3240.
- [77] R.L. Weiher, R.P. Ley, Optical properties of indium oxide, *J. Appl. Phys.* 37 (1966) 299.
- [78] A. Walsh, J.L.F. Da Silva, S.-H. Wei, C. Körber, A. Klein, L.F.J. Piper, A. DeMasi, K.E. Smith, G. Panaccione, P. Torelli, D.J. Payne, A. Bourlange, R.G. Egdell, Nature of the band gap of In_2O_3 revealed by first-principles calculations and X-ray spectroscopy, *Phys. Rev. Lett.* 100 (2008) 167402.
- [79] M. Feneberg, J. Nixdorf, C. Lidig, R. Goldhahn, Many-electron effects on the dielectric function of cubic In_2O_3 : effective electron mass, band nonparabolicity, band gap renormalization, and Burstein-Moss shift, *Phys. Rev. B* 93 (2016) 045203.
- [80] H. Odaka, S. Iwata, N. Taga, S. Ohnishi, Y. Kaneta, Y. Shigesato, Study on electronic structure and optoelectronic properties of indium oxide by first-principles calculations, Part 1, *Jpn. J. Appl. Phys.* 36 (1997) 5551.
- [81] I. Tanaka, M. Mizuno, H. Adachi, Electronic structure of indium oxide using cluster calculations, *Phys. Rev. B* 56 (1997) 3536.
- [82] E.A. Albanesi, S.J. Sferco, I. Lefebvre, G. Allan, M. Lannoo, Electronic structure of crystalline InP oxides, *Solid State Commun.* 86 (1993) 27–31.
- [83] P. Erhart, A. Klein, R.G. Egdell, K. Albe, Band structure of indium oxide: indirect versus direct band gap, *Phys. Rev. B* 75 (2007) 153205.
- [84] D. Vogel, P. Krüger, J. Pollmann, Self-interaction and relaxation-corrected pseudopotentials for II–VI semiconductors, *Phys. Rev. B* 54 (1996) 5495.
- [85] V.I. Anisimov, J. Zaanen, O.K. Andersen, Band theory and Mott insulators: Hubbard U instead of Stoner I, *Phys. Rev. B* 44 (1991) 943.
- [86] R.A. Pollak, S. Kowalczyk, L. Ley, D.A. Shirley, Evolution of core states from energy bands in the 4d5s5p region from Pd to Xe, *Phys. Rev. Lett.* 29 (1972) 274.

- [87] T. Kendelewicz, P.H. Mahowald, K.A. Bertness, C.E. McCants, I. Lindau, W.E. Spice, Surface shifts in the In 4d and P 2p core-level spectra of $\text{InP}(110)$, *Phys. Rev. B* 36 (1987) 6543.
- [88] S.L. Dudarev, G.A. Botton, S.Y. Savrasov, C.J. Humphreys, A.P. Sutton, Electron-energy-loss spectra and the structural stability of nickel oxide: an LSDA+U study, *Phys. Rev. B* 57 (1998) 1505.
- [89] A. Klein, Electronic properties of In_2O_3 surfaces, *Appl. Phys. Lett.* 77 (2000) 2009.
- [90] T.L. Barr, Y.L. Liu, An x-ray photoelectron spectroscopy study of the valence band structure of indium oxides, *J. Phys. Chem. Solids* 50 (1989) 657–664.
- [91] C. McGuinness, C.B. Stagescu, P.J. Ryan, J.E. Downes, D. Fu, K.E. Smith, R.G. Egdell, Influence of shallow core-level hybridization on the electronic structure of post-transition-metal oxides studied using soft X-ray emission and absorption, *Phys. Rev. B* 68 (2003) 165104.
- [92] S.Z. Karazhanov, P. Ravindran, P. Vajeeston, A. Ulyashin, T.G. Finstad, H. Fjellvåg, Phase stability, electronic structure, and optical properties of indium oxide polytypes, *Phys. Rev. B* 76 (2007) 075129.
- [93] P. Ágoston, K. Albe, R.M. Nieminen, M.J. Puska, Intrinsic *n*-type behavior in transparent conducting oxides: a comparative hybrid-functional study of In_2O_3 , SnO_2 , and ZnO , *Phys. Rev. Lett.* 103 (2009) 245501.
- [94] L.-M. Tang, L.-L. Wang, D. Wang, J.-Z. Liu, K.-Q. Chen, Donor-donor binding in In_2O_3 : engineering shallow donor levels, *J. Appl. Phys.* 107 (2010) 083704.
- [95] S. Limpijumong, P. Reunchan, A. Janotti, C.G. Van de Walle, Hydrogen doping in indium oxide: an ab initio study, *Phys. Rev. B* 80 (2009) 193202.
- [96] T. Koida, H. Fujiwara, M. Kondo, Hydrogen-doped In_2O_3 as high-mobility transparent conductive oxide, *Jpn. J. Appl. Phys.* 46 (2007) L685.
- [97] T. Koida, H. Fujiwara, M. Kondo, Structural and electrical properties of hydrogen-doped In_2O_3 films fabricated by solid-phase crystallization, *J. Noncryst. Solids* 354 (2008) 2805–2808.
- [98] P.D.C. King, R.L. Lichti, Y.G. Celebi, J.M. Gil, R.C. Vilao, H.V. Alberto, J.P. Duarte, D.J. Payne, R.G. Egdell, I. McKenzie, C.F. McConville, S.F.J. Cox, T.D. Veal, Shallow donor state of hydrogen in In_2O_3 and SnO_2 : implications for conductivity in transparent conducting oxides, *Phys. Rev. B* 80 (2009) 081201 (R).
- [99] M. Stavola, F. Bekisli, W. Yin, K. Smithe, W.B. Fowler, L.A. Boatner, Contrasting the experimental properties of hydrogen in SnO_2 , In_2O_3 , and TiO_2 , *J. Appl. Phys.* 115 (2014) 012001.
- [100] Y. Meng, X. Yang, H. Chen, J. Shen, Y. Jiang, Z. Zhang, Z. Hua, Molybdenum-doped indium oxide transparent conductive thin films, *J. Vac. Sci. Technol. A* 20 (2002) 288–290.
- [101] A.E. Delahoy, S.Y. Guo, Transparent and semitransparent conducting film deposition by reactive-environment, hollow cathode sputtering, *J. Vac. Sci. Technol. A* 23 (2005) 1215–1220.
- [102] P.F. Newhouse, C.-H. Park, D.A. Keszler, J. Tate, P.S. Nyholm, High electron mobility W-doped In_2O_3 thin films by pulsed laser deposition, *Appl. Phys. Lett.* 87 (2005) 112108.
- [103] T. Koida, M. Kondo, High-mobility transparent conductive Zr-doped In_2O_3 , *Appl. Phys. Lett.* 89 (2006) 082104.
- [104] O. Bierwagen, J.S. Speck, Plasma-assisted molecular beam epitaxy of Sn-doped In_2O_3 : Sn incorporation, structural changes, doping limits, and compensation, *Phys. Status Solidi A* 211 (2014) 48–53.

- [105] R.L. Weiher, Electrical properties of single crystals of indium oxide, *J. Appl. Phys.* 33 (1926) 2834.
- [106] J.H.W. de Wit, The high temperature behavior of In_2O_3 , *J. Solid State Chem.* 13 (1975) 192–200.
- [107] O. Bierwagen, J.S. Speck, Mg acceptor doping of In_2O_3 and overcompensation by oxygen vacancies, *Appl. Phys. Lett.* 101 (2012) 102107.
- [108] E. Korhonen, F. Tuomisto, O. Bierwagen, J.S. Speck, Z. Galazka, Compensating vacancy defects in Sn- and Mg-doped In_2O_3 , *Phys. Rev. B* 90 (2014) 245307.
- [109] Y. Hao, G. Meng, C. Ye, L. Zhang, Controlled synthesis of In_2O_3 octahedrons and nanowires, *Cryst. Growth Des.* 5 (2005) 1617–1621.
- [110] K. Tomioka, M. Yoshimura, T. Fukui, A III-V nanowire channel on silicon for high-performance vertical transistors, *Nature* 488 (2012) 189–192.
- [111] S. Maeda, K. Tomioka, S. Hara, J. Motohisa, Fabrication and characterization of InP nanowire light-emitting diodes, *Jpn. J. Appl. Phys.* 51 (2012) 02BN03.
- [112] M. Higashiwaki, K. Sasaki, A. Kuramata, T. Masui, S. Yamakoshi, Gallium oxide (Ga_2O_3) metal-semiconductor field-effect transistors on single-crystal β - Ga_2O_3 (010) substrates, *Appl. Phys. Lett.* 100 (2012) 013504.